Contribution to special issue dedicated to Paul Heitjans

Olena Porodko, Martin Fabián*, Hristo Kolev, Maksym Lisnichuk, Markéta Zukalová, Monika Vinarčíková, Vladimír Girman, Klebson Lucenildo Da Silva and Vladimír Šepelák

A novel high entropy spinel-type aluminate MAl_2O_4 (M = Zn, Mg, Cu, Co) and its lithiated oxyfluoride and oxychloride derivatives prepared by one-step mechanosynthesis

https://doi.org/10.1515/zpch-2021-3106
Received July 30, 2021; accepted September 20, 2021; published online October 4, 2021

Abstract: For the first time, a spinel-type high entropy oxide $(Zn_{0.25}Cu_{0.25}Mg_{0.25}Co_{0.25})Al_2O_4$ as well as its derivative lithiated high entropy oxyfluoride $Li_{0.5}(Zn_{0.25}Cu_{0.25}Mg_{0.25}Co_{0.25})_{0.5}Al_2O_{3.5}F_{0.5}$ and oxychloride $Li_{0.5}(Zn_{0.25}Cu_{0.25}Mg_{0.25}Co_{0.25})_{0.5}Al_2O_{3.5}Cl_{0.5}$ are prepared in the nanostructured state via high-energy co-milling of the simple oxide precursors and the halides (LiF or LiCl) as sources of lithium, fluorine and chlorine. Their nanostructure is investigated by XRD, HR-TEM, EDX and XPS spectroscopy. It is revealed that incorporation of lithium into the structure of spinel oxide together with the anionic substitution has significant effect on its short-range order, size and morphology of crystallites as well as on its oxidation/reduction

***Corresponding author: Martin Fabián**, Institute of Geotechnics, Slovak Academy of Sciences, Košice, Slovakia, E-mail: fabianm@saske.sk
Olena Porodko, Institute of Geotechnics, Slovak Academy of Sciences, Košice, Slovakia
Hristo Kolev, Institute of Catalysis, Bulgarian Academy of Sciences, Sofia, Bulgaria
Maksym Lisnichuk and Vladimír Girman, Institute of Physics, P. J. Šafárik University, Košice, Slovakia
Markéta Zukalová and Monika Vinarčíková, J. Heyrovský Institute of Physical Chemistry, Academy of Sciences of the Czech Republic, v.v.i., Prague, Czech Republic
Klebson Lucenildo Da Silva, Institute of Geotechnics, Slovak Academy of Sciences, Košice, Slovakia; Institute of Nanotechnology, Karlsruhe Institute of Technology, Eggenstein-Leopoldshafen, Karlsruhe, Germany; and Department of Physics, State University of Maringá, Maringá, Brazil
Vladimír Šepelák, Institute of Geotechnics, Slovak Academy of Sciences, Košice, Slovakia; and Institute of Nanotechnology, Karlsruhe Institute of Technology, Eggenstein-Leopoldshafen, Karlsruhe, Germany

processes. The charge capacity of the as-prepared nanomaterials tested by cyclic voltammetry is found to be rather poor despite lithiation of the samples in comparison to previously reported spinel-type high entropy oxides. Nevertheless, the present work offers the alternative one-step mechanochemical route to novel classes of high entropy oxides as well as to lithiated oxyfluorides and oxychlorides with the possibility to vary their cationic and anionic elemental composition.

Keywords: high-entropy spinel; lithiation; mechanosynthesis; oxychloride; oxyfluoride.

1 Introduction

Nowadays, new classes of materials are being intensely developed in order to fulfil requirements of present challenges. Among others, high entropy materials containing five or more elements in near-equiatomic ratios with the concept of well-known high entropy alloys (HEAs) offer promising solutions. Since their development in 2005, many research centres have focused their interest to expand this field of multi-component materials [1]. The unique properties of HEAs motivated further exploration towards high entropy nitrides, oxides (HEOs), metal diborides, carbides, sulfides, fluorides and very recently aluminosilicates [2].

In particular, HEOs have attracted consideration due to their several unique technical applications in conjunction with, *e.g.*, dielectric [3], energy storage [4], magnetic [5], catalytic [6], electrical/thermal conductivity [7, 8], mechanical [9] and optical properties [10]. The first synthesis of a single phase HEO with rocksalt structure was reported by Rost et al. in 2015 [11]. It has prompted the interest to prepare various classes of simple or complex oxides including fluorite, bixbyite, perovskite, spinel, monoclinic, magnetoplumbite, pyrochlore, rutile and defect fluorite structures [2]. Together with recent progress in development of novel attractive electrode materials for next-generation lithium-ion batteries (LIBs), spinel-type HEOs have been characterized by robust lithium storage capacity. It is known that spinel structure (see Figure 1) possesses typical electrode architecture with a huge contribution of free spaces for ion pathways [12].

To the best of our knowledge, there are only few reports on LIB electrode candidates from the family of spinel-type HEOs including, *e.g.*, $(Mg_{0.2}Ti_{0.2}Zn_{0.2}Cu_{0.2}Fe_{0.2})_3O_4$ [13], $(Ni_{0.2}Co_{0.2}Mn_{0.2}Fe_{0.2}Ti_{0.2})_3O_4$ [14], $(FeCoNiCrMn)_3O_4$ [12, 15], as well as oxygen-deficient $(CoCrFeMnNi)_{0.6}O_{4-\delta}$ and $(Al_{0.2}CoCrFeMnNi)_{0.58}O_{4-\delta}$ [16]. It is assumed that spinel structure is characterized by its unique three-dimensional Li^+ transport pathways [15] due to the two different Wyckoff sites for cations, *i.e.*, tetrahedrally coordinated (A) and octahedrally coordinated [B] sites. This

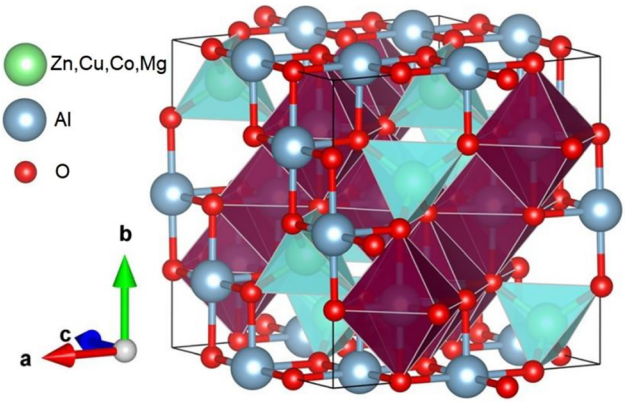

Figure 1: Idealized spinel structure of $(Zn_{0.25}Cu_{0.25}Mg_{0.25}Co_{0.25})Al_2O_4$. Octahedra and tetrahedral are occupied by Al and Zn, Cu, Co, Mg cations, respectively.

allows for the existence of trivalent cations, which can increase the range of valence state variation and thus the reversible capacity during the lithiation/delithiation process. On top of that, the particular cations can be distributed within the (A) and [B] sites of the spinel lattice and thus might result in various valence states of other constituent cations and in the formation of oxygen vacancies. The latter increases the configurational entropy and thus promotes Li^+ transport [17] taking place by Li-ion hopping between tetrahedral and octahedral sites. The transport through the Wyckoff spinel positions 8a(A) → 16c[B] → 8a(A) provides the shortest and energetically most favourable pathway for expected fast diffusion [18]. Apart from the transition metal (TM)-containing high entropy spinels, a high-density Li-doped $MgAl_2O_4$ has also been investigated as a potential solid electrolyte for an all-spinel Li-ion battery [19]. Although its Li-ion conductivity was found to be very low, the study reflected the necessity of further investigation of TM-containing spinels as potential candidates for Li-ion batteries components. In order to modify electrochemical performance of high entropy materials, Wang et al. [20] introduced a new class of high entropy materials, *i.e.*, rocksalt-type lithiated oxyfluorides, $Li_x(Co_{0.2}Cu_{0.2}Mg_{0.2}Ni_{0.2}Zn_{0.2})OF_x$, as promising candidates for energy storage applications based on multi-anionic and -cationic compounds.

In our previous work [21–23] nanostructured spinel oxides in a far-from-equilibrium structural state have been prepared by means of mechanochemical routes. The potential of mechanochemistry to have paradigm-changing impact across the chemical sciences has placed the field amongst IUPAC's '10 chemical innovations that will change our world' [24]. Motivated by the present interest in spinel-type HEO materials, here we report, for the first time, on the mechanosynthesis of the high

entropy spinel oxide $(Zn_{0.25}Cu_{0.25}Mg_{0.25}Co_{0.25})Al_2O_4$ and its lithiated derivatives of oxyfluoride $Li_{0.5}(Zn_{0.25}Cu_{0.25}Mg_{0.25}Co_{0.25})_{0.5}Al_2O_{3.5}F_{0.5}$ and oxychloride $Li_{0.5}(Zn_{0.25}Cu_{0.25}Mg_{0.25}Co_{0.25})_{0.5}Al_2O_{3.5}Cl_{0.5}$. Despite the multi-element composition of the as-synthesized samples, the easy-to-handle one-step process of mechanosynthesis provides phase-pure spinel products in the nanocrystalline state. By means of the combination of diffraction (Rietveld analysis of XRD data), spectroscopy (XPS) and microscopy (HR-TEM) the detailed structural information on the mechano-synthesized nanomaterials is provided. Moreover, the electrochemical behaviour (charge capacity) of the as-synthesized samples is investigated by cyclic voltammetry.

2 Experimental

The high entropy spinel-type $(Zn_{0.25}Cu_{0.25}Mg_{0.25}Co_{0.25})Al_2O_4$ (further denoted as HEOAl) was synthesized by high-energy ball milling of stoichiometric mixtures of metal oxide precursors: zinc (II) oxide (ZnO, 99.9%, Sigma Aldrich), copper (II) oxide (CuO, 99.9%, Acros Organics), magnesium oxide (MgO, 99.9%, Acros Organics), cobalt (II) oxide (CoO prepared by thermal decomposition of $Co(OH)_2$, 95%, Acros Organics, at 180 °C in vacuum) and aluminium (III) oxide (γ-Al_2O_3, 99.9%, Sigma Aldrich). Milling experiments were carried out in air atmosphere at 600 rpm using a Pulverisette 7 Premium Line (Fritsch) planetary mill with vial (80 cm^3 in volume) and balls (10 mm in diameter) made of tungsten carbide. The ball-to-powder ratio was 30:1 (corresponding to 5 g of the starting precursors and 150 g of balls). The lithiated oxyfluoride and oxychloride were prepared by co-milling of the above mentioned metal oxide precursors with lithium (I) fluoride (LiF, 99.9%, Acros Organics) and lithium (I) chloride (LiCl, 98%, Alfa Aesar), respectively, in stoichiometric amounts under the same reaction conditions. The estimated chemical composition of the final lithiated products was $Li_{0.5}(Zn_{0.25}Cu_{0.25}Mg_{0.25}Co_{0.25})_{0.5}Al_2O_{3.5}F_{0.5}$ (further denoted as LiHEOAlF) and $Li_{0.5}(Zn_{0.25}Cu_{0.25}Mg_{0.25}Co_{0.25})_{0.5}Al_2O_{3.5}Cl_{0.5}$ (LiHEOAlCl).

The mechanically induced phase evolution was monitored by XRD using a D8 Advance X-ray diffractometer (Bruker), operating in Bragg configuration and using Cu Kα radiation. The XRD scans were collected from 20° to 80° (2 Theta), using a step of 0.04° and scan rate of 10 s/step. The phase identification was utilized by the ICSD database [25]. The Rietveld refinement of the XRD data was performed using *FullProf Suite* software [26] and LaB_6 as an internal standard for the accurate lattice parameter determination. The average crystallite size was estimated by the Williamson-Hall plot analysis of XRD data [27].

The morphology of powders was investigated using a combined field-emission (scanning) transmission electron microscope (S)TEM (JEOL JEM-2100 UHR) operated at 200 kV, equipped with EDX detector (Oxford Instruments). The (S)TEM-bright field mode was used for imaging of powders. For (S)TEM analysis, the powdered samples were diluted in distilled water and ultrasonicated. The crystallite size distribution was evaluated using the *ImageJ* software [28].

X-ray photoelectron spectroscopic measurements were carried out using the ESCALAB MkII (VG Scientific) spectrometer at a base pressure inside the analysis chamber of 5×10^{-10} mbar. A twin anode MgKα/AlKα X-ray source was used with excitation energies of 1253.6 and 1486.6 eV,

respectively. The spectra were recorded at the total instrumental resolution (as it was measured with the FWHM of $Ag3d_{5/2}$ photoelectron line) of 1.06 and 1.18 eV for MgKα and AlKα excitation sources, respectively. The energy scale was calibrated by normalizing the C1s line of adsorbed adventitious hydrocarbons to 285.0 eV. The processing of the measured spectra includes a subtraction of X-ray satellites and Shirley-type background [29]. The peak positions and areas were estimated by a symmetrical Gaussian-Lorentzian curve fitting. The relative concentrations of chemical species were determined on the basis of normalization of the peak areas to their photoionization cross-sections, calculated by Scofield [30].

For electrochemical measurements, the powdered mechanosynthesized materials were mixed with C65 (carbon black, Timcal) in a mass ratio 4:1 and mortared carefully. The mixtures were then suspended in 2% carboxymethylcellulose in water to a consistency of viscous paste, stirred overnight and coated by doctor-blading on Al foil. After drying at room temperature and then in vacuum at 100 °C overnight the coated Al foil was cut into disc electrodes of 15 mm in diameter. The electrodes were stored in a glove box with Ar atmosphere. Electrochemical measurements were carried out using Autolab 302N apparatus (Metrohm) controlled by Nova SW in a Swagelok-type cell with Li-metal anode, polypropylene separator (Targray) and 1 M $LiPF_6$ in ethylene carbonate/dimethyl carbonate (1:1 by volume) as an electrolyte in an Ar-filled glove box.

3 Results and discussion

As it is seen in Figure 2, the XRD pattern for the starting (unmilled) ZnO + CuO + MgO + CoO + γ-Al_2O_3 mixture is characterized by sharp diffraction peaks corresponding to the ZnO, CuO and MgO precursors. The diffraction peaks of CoO and γ-Al_2O_3 are not visible due to their amorphous character. After 10 min of ball milling the diffraction peaks become broadened and with increasing milling time, several diffraction peaks (denoted by Miller indices *hkl*) can be attributed to the formed spinel phase. After 60 min of mechanical treatment, the majority of diffraction peaks above the background belongs to the mechanosynthesized HEOAl. The mechanochemical formation reaction is completed after 390 min of intensive ball milling; the spinel phase is represented here by fully symmetrical diffraction peaks. Thus, the present mechanosynthesis of HEOAl can be expressed by the following chemical reaction:

$$0.25\,\mathrm{ZnO} + 0.25\,\mathrm{CuO} + 0.25\,\mathrm{MgO} + 0.25\,\mathrm{CoO} + \gamma\text{–}\mathrm{Al_2O_3} \rightarrow (\mathrm{Zn_{0.25}Cu_{0.25}Mg_{0.25}Co_{0.25}})\mathrm{Al_2O_4} \quad (1)$$

Accordingly, the XRD patterns of the lithiated samples LiHEOAlF and LiHEOAlCl prepared by co-milling of the mechanosynthesized HEOAl with LiF and LiCl, respectively, are shown in Figure 3. The XRD peaks are attributed to the spinel structure (S.G. *Fd3m*). In this context, the mechanochemically induced formation

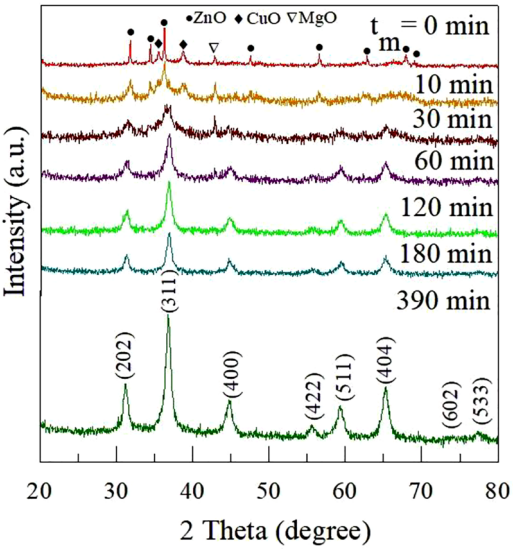

Figure 2: XRD patterns of the mixture of oxide precursors (ZnO + CuO + MgO + CoO + γ-Al_2O_3) milled for various times (up to 390 min). The milling time, t_m, is shown in the figure. Note that diffraction peaks of highly porous γ-Al_2O_3 and CoO are not visible due to amorphous nature of the oxides. Diffraction peaks of the final product $(Zn_{0.25}Cu_{0.25}Mg_{0.25}Co_{0.25})Al_2O_4$ are denoted by Miller indices.

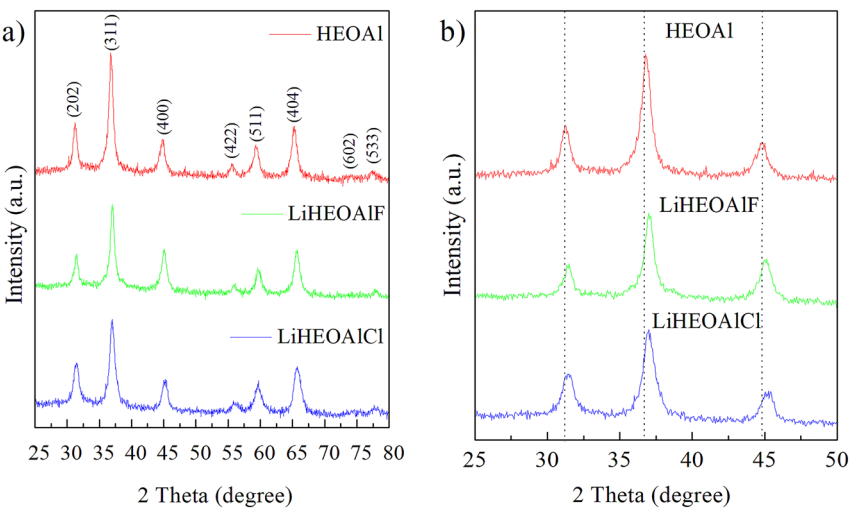

Figure 3: Comparison of the XRD patterns of mechanosynthesized HEOAl, LiHEOAlF and LiHEOAlCl in the range (a) from 25° to 80° and (b) from 25° to 50° (2 Theta). Vertical lines represent a guide to eye to accent a shift of XRD peaks due to the formation of the particular Li-doped oxyfluoride and oxychloride.

of LiHEOAlF and LiHEOAlCl crystallites can be described by the following reactions:

$$0.5\,LiF + 0.125\,ZnO + 0.125\,CuO + 0.125\,MgO + 0.125\,CoO + \gamma\text{–}Al_2O_3 \rightarrow Li_{0.5}Zn_{0.125}Cu_{0.125}Mg_{0.125}Co_{0.125}Al_2O_{3.5}F_{0.5} \quad (2)$$

and

$$0.5\,LiCl + 0.125\,ZnO + 0.125\,CuO + 0.125\,MgO + 0.125\,CoO + \gamma\text{–}Al_2O_3 \rightarrow Li0.5Zn_{0.125}Cu_{0.125}Mg_{0.125}Co_{0.125}Al_2O_{3.5}Cl_{0.5} \quad (3)$$

The XRD diffraction peaks for the mechanosynthesized compounds containing lithium and fluorine/chlorine are shifted towards higher degrees (2 Theta); see Figure 3b. It clearly demonstrates that the mechanochemically synthesized Li-containing high entropy spinels possess modified value of lattice parameter in comparison with that of the HEOAl sample. The crystal lattice parameters of the as-prepared materials derived from their XRD data are listed in Table 1. The observed lattice contraction is a consequence of both the incorporation of Li+ cations into the spinel structure with smaller Shannon radii (in comparison to that of M ions) [31] and the formation of oxygen defects for electroneutrality compensation. In addition, the broad shape of XRD peaks reflects the nanoscale character of the as-prepared spinels. Their average crystallite sizes estimated by Williamson-Hall plot analysis of XRD data are given in Table 1.

The representative STEM micrographs of the mechanosynthesized nanomaterials (Figure 4) show agglomerated state of nanoparticles with the average size ~ 16, 17 and 6 nm for HEOAl, LiHEOAlF and LiHEOAlCl, respectively. The selected area electron diffraction (SAED) patterns, presented in Figure 4, also confirm the presence of the HEOAl, LiHEOAlF and LiHEOAlCl spinel phases in the nanostructured state. In addition, the HR-TEM images reveal lattice fringes corresponding to the spinel crystallographic planes with the average interplanar distances $d_{(300)}$ = 2.7 Å, $d_{(110)}$ = 5.6 Å and $d_{(311)}$ = 2.4 Å for HEOAl, LiHEOAlF and LiHEOAlCl, respectively.

Table 1: The lattice parameter (*a*), interplanar distance (*d*) and average crystallite size (*D*) for HEOAl, LiHEOAlF and LiHEOAlCl.

Sample	Lattice parameter, *a* (Å)	Interplanar distance, *d* observed (Å)	Interplanar distance, *d* calculated (Å)	Crystallite size, D_{XRD} (nm)	Crystallite size, D_{TEM} (nm)
HEOAl	8.1024(3)	$2.7_{for\ (hkl\ =\ 300)}$	$2.7_{for\ (hkl\ =\ 300)}$	15	16
LiHEOAlF	8.0443(6)	$5.6_{for\ (hkl\ =\ 110)}$	$5.7_{for\ (hkl\ =\ 110)}$	15	17
LiHEOAlCl	8.0331(1)	$2.4_{for\ (hkl\ =\ 311)}$	$2.4_{for\ (hkl\ =\ 311)}$	11	6

The indices (*300*) and (*300*) belong to the forbidden XRD reflections and thus are observed by HR-TEM only.

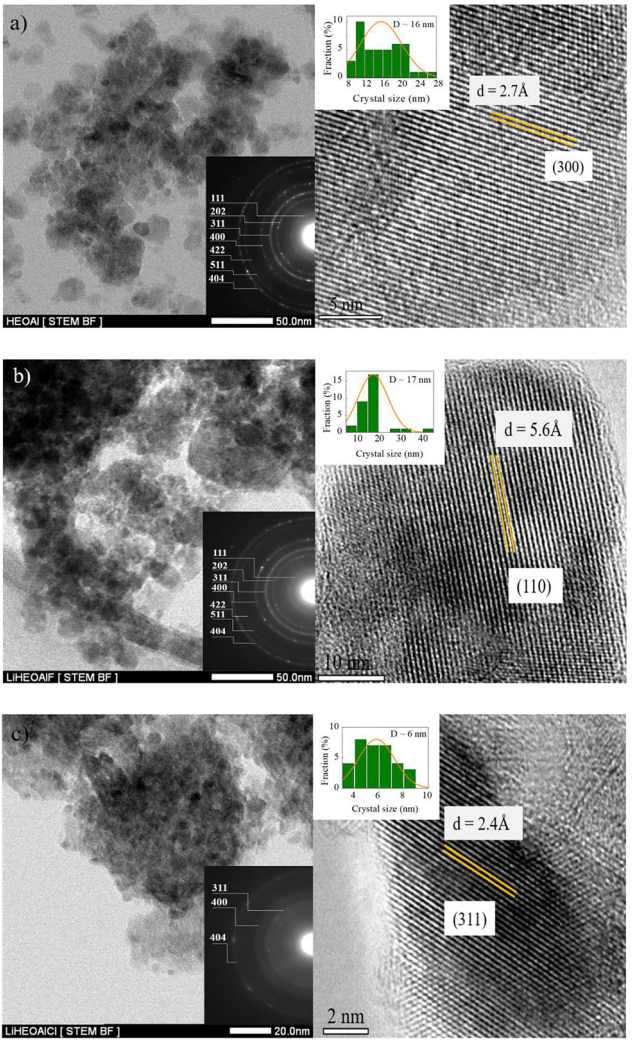

Figure 4: From left to right: STEM (inset: SAED) and HR-TEM micrographs (inset: crystallite size distribution) of the mechanosynthesized (a) HEOAl, (b) LiHEOAlF and (c) LiHEOAlCl. The interplanar distances, *d*, correspond to the particular spinel crystallographic planes denoted by Miller indices.

For comparison, the values of interplanar distances $d_{(hkl)}$ were also calculated from the values of lattice parameter (a) derived from Rietveld refinement of XRD data according to the formula:

$$1/d^2_{(hkl)} = \left(h^2 + k^2 + l^2\right)/a^2 \tag{4}$$

It is evident (see Table 1) that estimated *d* values are in well agreement with those directly observed in HR-TEM micrographs. Figure 5 displays the EDX mapping of Al, Co, Cu, Zn, Mg, O, F and Cl elements present in the mechanosynthesized nanomaterials. The EDX analyses reveal a homogeneous distribution of the constituent elements within the as-prepared spinels.

The high-resolution XPS measurements of the as-prepared nanomaterials were performed to investigate the effect of the mechanochemical preparation method on the oxidation state of the constituent elements. As it is shown in Figure 6, the oxidation-reduction processes took place during the mechanosyntheses, and various oxidation states of several elements are revealed. In the case of Al2p (Figure 6a), the measured binding energies in the range of 74.0–74.5 eV are typical for Al^{3+} in Al–O bonds [32, 33].

The two different oxidation states of cobalt (analysis of $Co2p_{1/2}$), *i.e.*, Co^{2+} located at ~ 797.3 eV and Co^{3+} located at ~ 796.0 eV are distinguished in the spectrum of the nanomaterials (see Figure 6b). In addition, the satellite for both peaks can be observed at + ~ 6.5 eV for Co^{2+} and + ~ 9 eV for Co^{3+} [34, 35]. It is evident from quantitative data summarized in Table 2 that the Co^{2+}/Co^{3+} ratio decreases as the Li and F/Cl are incorporated into the structure of HEOAl. The main $Cu2p_{3/2}$ peak is located at 933.1–933.9 eV (Figure 6c). The shape of the satellite peak located at ~ 942.5 eV indicates that the reduction of Cu (from Cu^{2+} to Cu^{1+}) is facilitated by the Li and Cl incorporation [36]. On the other hand, the oxidation states of Zn (Zn2p at ~ 1021.4 eV) and Mg (Mg1s at ~ 1303.5 eV) are not affected by

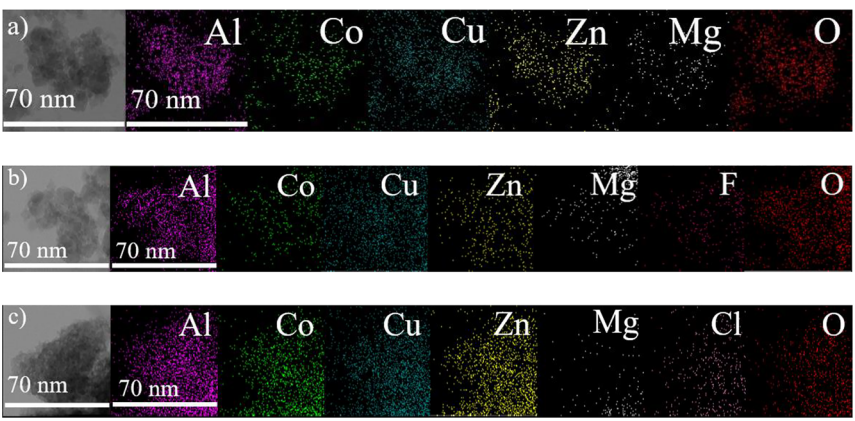

Figure 5: The EDX mapping of (a) HEOAl, (b) LiHEOAlF and (c) LiHEOAlCl. The micrographs show a homogeneous distribution of the constituent elements within the as-prepared high entropy nanomaterials.

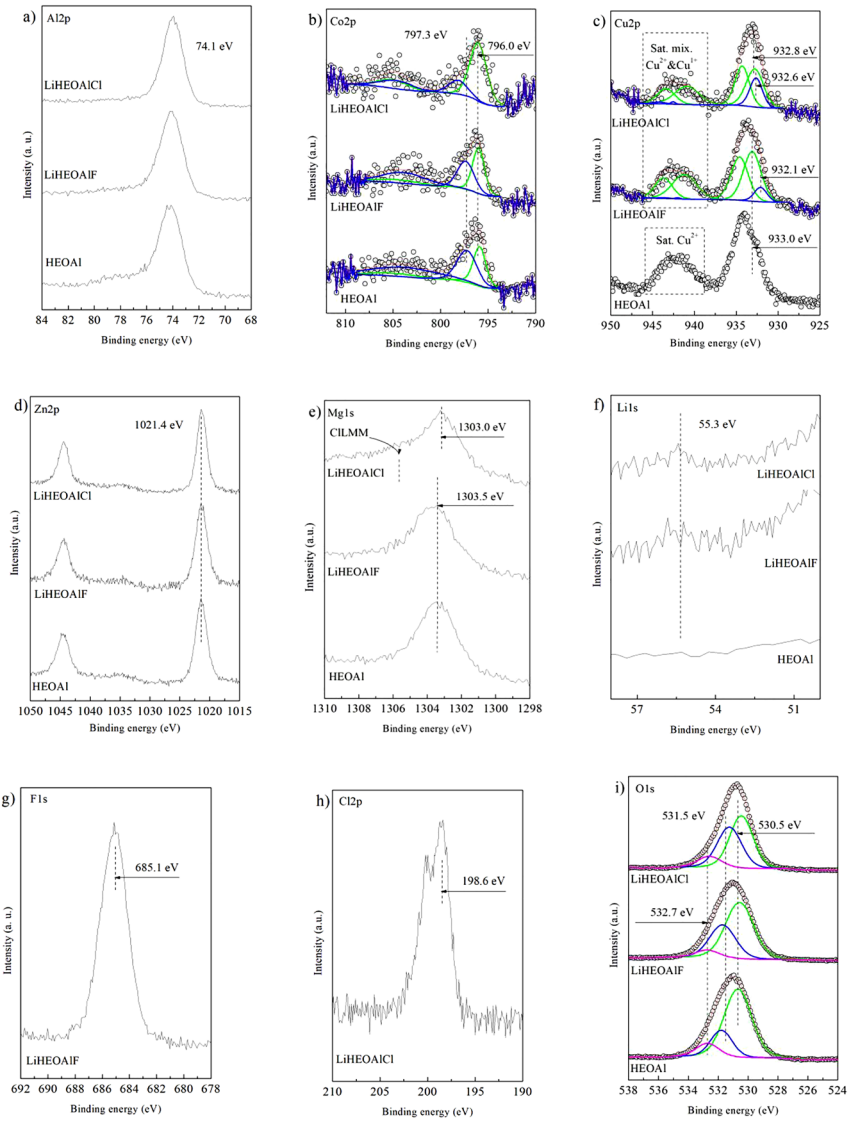

Figure 6: High-resolution XPS spectra of the mechanosynthesized HEOAl, LiHEOAlF and LiHEOAlCl compounds showing the signals corresponding to (a) Al2p, (b) Co2p, (c) Cu2p, (d) Zn2p, (e) Mg1s, (f) Li1s, (g) F1s, (h) Cl2p and (i) O1s. Note that XPS spectra of Mg1s are partly overlapped with the subspectrum of Cl Auger electrons.

the elemental composition of the samples [37, 38], see Figure 6d and e, respectively. The Li1s (at ~ 55.3 eV) was determined for lithiated samples (Figure 6f). The binding energies of the F1s (at ~ 685.1 eV) and Cl2p (at ~ 198.6 eV) subspectra shown in Figure 6g and h, respectively, correspond to the metal–fluoride and metal–chloride bonds, respectively [39, 40]. The O1s peak (Figure 6i) can be fitted into three regions; the peak located at ~ 530.5 eV is attributed to the typical metal–oxygen bond, the peak located at ~ 532.7 eV represents the chemically and physically adsorbed water on the sample surface and the peak centred at ~ 531.5 eV is connected with oxygen defect sites with low oxygen coordination [41]. The peak related to the formation of oxygen vacancies increases in intensity as Li and F/Cl are incorporated into HEOAl and becomes the most dominant in the spectrum for LiHEOAlCl (see Table 2). Thus, the incorporation of Li and F/Cl creates more defective structure of crystals and increases the concentration of defects. However, in the present study it is difficult to distinguish the origin of progress in oxidation and reduction processes of particular elements in LiHEOAlF and LiHEOAlCl samples.

The electrochemical performance of the HEOAl, LiHEOAlF and LiHEOAlCl samples is investigated by cyclic voltammetry of Li insertion in the potential window of 0.01–3.0 V versus Li^+/Li at a scan rate of 0.1 mV s^{-1} as shown in Figure 7. The charge capacity of HEOAl determined from the cyclic voltammogram is found to be 54 mAh g^{-1}. The value of the charge capacity slightly increased for LiHEOAlF (to about 71 mAh g^{-1}), while there is no significant effect of lithiation and anionic exchange observed in LiHEOAlCl, whose charge capacity is found to be about 52 mAh g^{-1}. It should be noted that the estimated values of the charge capacity for the mechanosynthesized HEOAl, LiHEOAlF and LiHEOAlCl spinels are significantly lower in comparison to those reported for spinel-type HEOs in Refs [12–16].

Despite this fact, the main message of the present study is that one-step mechanosynthesis is capable to deliver nanocrystalline high entropy spinel oxides with various chemical composition including lithiated high entropy oxyfluorides/oxychlorides and opens the pathway towards further optimization of synthesis resulting in improved charge capacity of the products.

Table 2: The Co^{2+}/Co^{3+} and Cu^{2+}/Cu^{1+} ratios as well as the O^{2-} vacancy concentration in the mechanosynthesized HEOAl, LiHEOAlF and LiHEOAlCl compounds determined by XPS analysis.

	HEOAl	LiHEOAlF	LiHEOAlCl
Co^{2+}/Co^{3+} (at.%)	0.42/0.22	0.16/0.12	0.10/0.21
Cu^{2+}/Cu^{1+} (at.%)	–	0.86/0.07	0.11/0.53
O^{2-} (vacancy) (at.%)	12.50	16.69	22.01

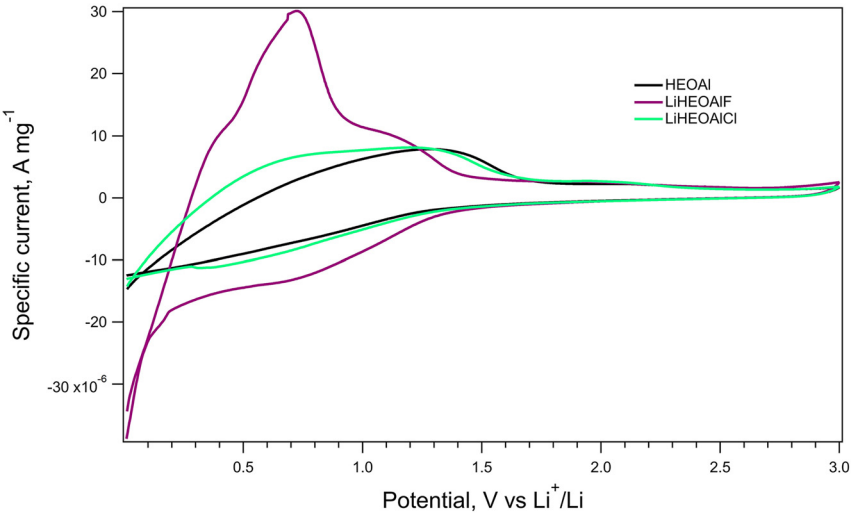

Figure 7: Cyclic voltammogram of Li insertion into the HEOAl, LiHEOAlF and LiHEOAlCl samples at a scan rate of 0.1 mV s^{-1}.

4 Conclusions

The spinel-type high entropy aluminate $(Zn_{0.25}Cu_{0.25}Mg_{0.25}Co_{0.25})Al_2O_4$ as well as the spinel-type lithiated oxyfluoride $Li_{0.5}(Zn_{0.25}Cu_{0.25}Mg_{0.25}Co_{0.25})_{0.5}Al_2O_{3.5}F_{0.5}$ and oxychloride $Li_{0.5}(Zn_{0.25}Cu_{0.25}Mg_{0.25}Co_{0.25})_{0.5}Al_2O_{3.5}Cl_{0.5}$ were prepared for the first time by mechanosynthesis. The contracted cubic lattice observed for both oxyfluoride and oxychloride is a consequence of the incorporation of Li^+ cations into the spinel structure and the formation of oxygen vacancies. These structural variations derived from Rietveld refinements of XRD data are also supported at the local scale by HR-TEM. The latter reveals the nanostructured state of the as-prepared spinels with the average crystallite size of about 16, 17 and 6 nm for the aluminate, oxyfluoride and oxychloride, respectively. The homogeneous distribution of the constituent elements within the high entropy nanospinels is confirmed by EDX analyses. The results of XPS measurements reveal various oxidation states of several constituent elements as well as different concentrations of oxygen vacancies in high entropy spinels, depending on their chemical composition and crystallites size. The mechanosynthesized spinel-type nanomaterials exhibit a relatively low charge capacity when compared to that reported for other spinel-type high entropy oxides.

Author contributions: All the authors have accepted responsibility for the entire content of this submitted manuscript and approved submission.
Research funding: This work was supported by the APVV (19-0526), the VEGA (2/0055/19) and the bilateral cooperation BAS-SAS (21-07). M.Z. and M.V. thank the Grant Agency of the Czech Republic (20-03564S) for supporting their research work. V.Š. acknowledges the support by the DFG (SE 1407/4-2).
Conflict of interest statement: The authors declare no conflicts of interest regarding this article.

References

1. Yeh J.-W., Chen S.-K., Lin S.-J., Gan J.-Y., Chin T.-S., Shun T.-T., Tsau C.-H., Chang S.-Y. *Adv. Eng. Mater.* 2004, *6*, 299–303.
2. Musicó B. L., Gilbert D., Ward T. Z., Page K., George E., Yan J., Mandrus D., Keppens V. *APL Mater.* 2020, *8*, 040912.
3. Bérardan D., Franger S., Dragoe D., Meena A. K., Dragoe N. *Phys. Status Solidi Rapid Res. Lett.* 2016, *10*, 328–333.
4. Sarkar A., Velasco L., Wang D., Wang Q., Talasila G., de Biasi L., Kübel C., Brezesinski T., Bhattacharya S. S., Hahn H., Breitung B. *Nat. Commun.* 2018, *9*, 1–9.
5. Meisenheimer P. B., Williams L. D., Sung S. H., Gim J., Shafer P., Kotsonis G. N., Maria J., Trassin M., Hovden R., Kioupakis E., Heron J. T. *Phys. Rev. Mater.* 2019, *3*, 104420.
6. Chen H., Fu J., Zhang P., Peng H., Abney C. W., Jie K., Liu X., Chi M., Dai S. *J. Mater. Chem. A* 2018, *6*, 11129–11133.
7. Braun J. L., Rost C. M., Lim M., Giri A., Olson D. H., Kotsonis G. N., Stan G., Brenner D. W., Maria J.-P., Hopkins P. E. *Adv. Mater.* 2018, *30*, 1805004.
8. Balcerzak M., Kawamura K., Bobrowski R., Rutkowski P., Brylewski T. *J. Electron. Mater.* 2019, *48*, 7105–7113.
9. Ren K., Wang Q., Shao G., Zhao X., Wang Y. *Scr. Mater.* 2020, *178*, 382–386.
10. Zhang J., Zhang X., Li Y., Du Q., Liu X., Qi X. *Mater. Lett.* 2019, *244*, 167–170.
11. Rost C. M., Sachet E., Borman T., Moballegh A., Dickey E. C., Hou D., Jones J. L., Curtarolo S., Maria J.-P. *Nat. Commun.* 2015, *6*, 8485.
12. Wang D., Jiang S., Duan C., Mao J., Dong Y., Dong K., Wang Z., Luo S., Liu Y., Qi X. *J. Alloys Compd.* 2020, *844*, 156158.
13. Chen H., Qiu N., Wu B., Yang Z., Sun S., Wang Y. *RSC Adv.* 2020, *10*, 9736–9744.
14. Chen T., Wang S., Kuo C., Huang S., Lin M., Li C., Chen H., Wang C., Liao Y., Lin C., Chang Y., Yeh J., Lin S., Chen T., Chen H. *J. Mater. Chem. A* 2020, *8*, 21756–21770.
15. Nguyen T. X., Patra J., Chang J.-K., Ting J.-M. *J. Mater. Chem. A* 2020, *8*, 18963–18973.
16. Xiang H.-Z., Xie H.-X., Chen Y.-X., Zhang H., Mao A., Zheng C.-H. *J. Mater. Sci.* 2021, *56*, 8127–8142.
17. Bérardan D., Franger S., Meena A., Dragoe N. *J. Mater. Chem. A* 2016, *4*, 9536–9541.
18. Rosciano F., Pescarmona P. P., Houthoofd K., Persoons A., Bottke P., Wilkening M. *Phys. Chem. Chem. Phys.* 2013, *15*, 6107–6112.
19. Djenadic R., Botros M., Hahn H. *Solid State Ion.* 2016, *287*, 71–76.

20. Wang Q., Sarkar A., Wang D., Velasco L., Azmi R., Bhattacharya S. S., Bergfeldt T., Düvel A., Heitjans P., Brezesinski T., Hahn H., Breitung B. *Energy Environ. Sci.* 2019, *12*, 2433–2442.
21. Fabián M., Bottke P., Girman V., Düvel A., Da Silva K. L., Wilkening M., Hahn H., Heitjans P., Šepelák V. *RSC Adv.* 2015, *5*, 54321–54328.
22. Fabián M., Harničárová M., Valíček J., Da Silva K. L., Hahn H., Šepelák V., Lesňák M., Kušnerová M. *J. Nanosci. Nanotechnol.* 2019, *19*, 3654–3657.
23. Šepelák V., Düvel A., Wilkening M., Becker K. D., Heitjans P. *Chem. Soc. Rev.* 2013, *42*, 7507–7520.
24. Gomollón-Bel F. *Chem. Int.* 2019, *41*, 12–17.
25. *Inorganic Crystal Structure Database (ICSD)*; Leibniz Institute for Information Infrastructure, FIZ Karlsruhe: Karlsruhe, 2020.
26. Rodríguez-Carvajal J. *Fullprof Suite*; Institute Laue-Langevin: Grenoble, France, 2019.
27. Nath D., Singh F., Dasa R. *Mater. Chem. Phys.* 2020, *239*, 122021.
28. Schneider C. A., Rasband W. S., Eliceiri K. W. *Nat. Methods* 2012, *9*, 671–675.
29. Shirley D. *Phys. Rev. B* 1972, *5*, 4709–4714.
30. Scofield J. H. *J. Electron. Spectrosc. Relat. Phenom.* 1976, *8*, 129–137.
31. Shannon R. D. *Acta Crystallogr. A* 1976, *32*, 751–767.
32. Strohmeier B. R. *Surf. Interface Anal.* 1990, *15*, 51–56.
33. Gusmano G., Montesperelli G., Traversa E., Bearzotti A., Petrocco G., D'Amico A., Di Natale C. *Sensor. Actuator. B Chem.* 1992, *7*, 460–463.
34. Todorova S., Yordanova I., Naydenov A., Kolev H., Cherkezova-Zhelev Z., Tenchev K., Kunev B. *Rev. Roum. Chim.* 2014, *59*, 259–265.
35. Tyuliev G., Angelov S. *Appl. Surf. Sci.* 1988, *32*, 381–391.
36. Tomina V. V., Furtat I. M., Lebed A. P., Kotsyuda S. S., Kolev H., Kanuchova M., Melnyk I. V. *ACS Omega* 2020, *5*, 15290–15300.
37. Al-Gaashani R., Radiman S., Daud A. R., Tabet N., Al-Douri Y. *Ceram. Int.* 2013, *39*, 2283–2292.
38. Huang H.-H., Shih W.-C., Lai C.-H. *Appl. Phys. Lett.* 2010, *96*, 193505.
39. Cai J., Zhang Y., Qian Y., Shan C., Pan B. *Sci. Rep.* 2018, *8*, 1–10.
40. Tran M.-P., Gonzalez-Aguirre P., Beitia C., Lundgren J., Moon S.-I., Fontaine H. *Microelectron. Eng.* 2019, *207*, 1–6.
41. Lökçü E., Toparli Ç., Anik M. *ACS Appl. Mater. Interfaces* 2020, *12*, 23860–23866.